Dalton Transactions

Accepted Manuscript

ROYAL SOCIETY OF CHEMISTRY

www.rsc.org/dalton

Journal Name

ARTICLE

Multifunctional polyoxometalates encapsulated in MIL-100(Fe): highly efficient photocatalysts for selective transformation under visible light

Ruowen Liang,[a] Rui Chen,[a] Fenfen Jing,[a] Na Qin[a] and Ling Wu*[ab]

Received 00th January 20xx,
Accepted 00th January 20xx

DOI: 10.1039/x0xx00000x

www.rsc.org/

$H_3PMo_{12}O_{40}$ molecules have been successfully encapsulated in the cavities of MIL-100(Fe) *via* a facile hydrothermal method (denoted as HPMo@MIL-100(Fe)). A series of characterization has corroborated the insertion of $H_3PMo_{12}O_{40}$ within the cavities of MIL-100(Fe). The resulting HPMo@MIL-100(Fe) nanocomposites have exhibited much higher photoactivity than the original-MIL-100(Fe) toward photocatalytic selective oxidation of benzylic alcohols and reduction of Cr(VI) under visible light irradiation (λ ≥ 420 nm). The higher photoactivity of HPMo@MIL-100(Fe) can be attributed to the integrative effect of the enhanced light absorption intensity and more efficient separation of photogenerated electron-hole pairs. The host porous structure of MIL-100(Fe) can achieve uniform composition with the $H_3PMo_{12}O_{40}$, which is significantly important for producing highly reactive dispersed $H_3PMo_{12}O_{40}$ molecules and enhancing the photocatalytic activity of HPMo@MIL-100(Fe) nanocomposites. And the immobilized $H_3PMo_{12}O_{40}$ molecules are more convenient for recycling. Importantly, almost no Fe and Mo ions leach from the MIL-100(Fe) during the reaction, which verifies the photostability of the HPMo@MIL-100(Fe). In addiction, possible photocatalytic redox reactions mechanisms have been investigated.

1. Introduction

Polyoxometalates (POMs), as one kind of significant metal-oxide clusters with high negative charge and abundant topologies, have been employed in many research fields, such as optics, magnetism, biological medicine and catalysis.[1-4] Especially, some attempts have been made to explore the potential of POMs in the photocatalysis field. It has been reported that POMs can not only serve as homogeneous photocatalysts for the decolorization of organic dyes, [5] but also can project as ideal high-performance candidates for photocatalysts promoter by decreasing charge recombination.[6] However, they still suffer from some drawbacks like low surface area (1-10 m^2/g), low stability under catalytic conditions, and high solubility in aqueous solution is not convenient for recycling. Accordingly, some researchers have focused their efforts on the encapsulation of POMs within porous solid matrixes, such as SiO_2, Al_2O_3 and activated carbon.[7-11] Unfortunately, these routes typically result in low POMs loading, POMs leaching and the conglomeration of POMs particles. Therefore, it is of significance to search a suitable solid matrix to immobilize POMs, which might improve their photoactivities toward target reactions.

Metal-organic frameworks (MOFs) obtained by the assembly of metallic ions and organic ligands have attracted tremendous attention in the last two decades due to their high surface area, modular assembly, exceptional porosity and large specific surface area.[12-14] Since the historic work made by Ferey *et al.* on the direct encapsulation of POMs in MIL-101(Cr), a range of POM@MOFs nanocomposites have been discussed by researchers with great enthusiasm.[15-17] The superiority of using MOFs as support for POMs lie in the fact that (i) suitable cavities with the proper size allowing the dispersion of POMs at the molecular level and (ii) mild and simple synthesis conditions permitting the one-step

[a]*State Key Laboratory of Photocatalysis on Energy and Environment, Fuzhou University, Fuzhou 350002, China.*
[b]*State Key Laboratory of Structural Chemistry, Fujian Institute of Research on the Structure of Matter, Chinese Academy of Sciences, Fuzhou, Fujian 350002, China. E-mail: wuling@fzu.edu.cn. Phone: +86-591-83779362.*

† Electronic Supplementary Information (ESI) available: XRD patterns of calculated MIL-100(Fe); BET adsorption-desorption isotherm and Horvath-Kawazoe pore distribution of MIL-100(Fe) and HPMo@MIL-100(Fe); TEM image and EDX image of 30%HPMo@MIL-100(Fe); Mo/Fe ratio in the HPMo@MIL-100(Fe) nanocomposites determined by the ICP analysis; Reusability of 30%HPMo@MIL-100(Fe) for the photocatalytic selective oxidation of benzyl alcohol; XRD patterns of 30%HPMo@MIL-100(Fe) before and after the catalytic reaction; The concentration of Fe(III) and Mo(VI) during the reaction; Typical Mott-Schottky plots of MIL-100(Fe); UV-vis spectra of $H_3PMo_{12}O_{40}$; Zeta potential of MIL-100(Fe) as a function of pH value; Photocatalytic reduction of aqueous Cr(VI) over (1) MIL-100(Fe), (2) $H_3PMo_{12}O_{40}$, (3) 5%HPMo-MIL-100(Fe), (4) 5%HPMo@MIL-100(Fe) under the irradiation of visible light (λ ≥ 420 nm) for 8 min; The concentration of Fe(III) and Mo(VI) during the reaction; The photocatalytic reduction of Cr(VI) over 5%HPMo@MIL-100(Fe) under the visible light irradiation for 8 min in the presence of $AgNO_3$; Transient photocurrent response of MIL-100(Fe) and 5%HPMo@MIL-100(Fe) in 0.2 M Na_2SO_4 aqueous solution (pH 6.8); Photoluminescence (PL) spectra of MIL-100(Fe) and 5%HPMo@MIL-100(Fe); Nyquist impedance plots of MIL-100(Fe) and 5%HPMo@MIL-100(Fe). See DOI: 10.1039/x0xx00000x

encapsulation of the guest POMs.[12,13] For all these reasons, MOFs could be brilliant porous matrix to incorporate POMs. More importantly, it has been reported that some photoactive MOFs like MOF-5, UiO-66(NH_2) and MIL-53(Fe) behavior as semiconductors.[18-20] Therefore, it could be reasonably expected that a photoactive MOF can not only serve as a host to control the encapsulation of POMs, but also facilitate the separation of photogenerated charge carriers by forming the effective interfacial contact with POMs when the two components have well-matched band structures. Although there have been some reports on POM@MOFs. It should be noted that they always focus on the study of thermal catalysis or adsorption,[21-23] the reports on POM@MOFs for photocatalytic applications are rather scarce. Especially, the utilization of POM@MOFs as multifunctional photocatalysts in the selective transformation has remained unavailable so far.

MIL-100(Fe), a Fe(III) contained MOF built up from chains of Fe(III) octahedra and benzene-1,3,5-tricarboxylic acid, which has been chosen as the target supporter owing to its high chemical stability, water stability and photoresponsiveness.[24,25] Moreover, the two kinds of pores in the MIL-100(Fe) with free diameters of *ca.* 25 and 29 Å, accessible through the windows for *ca.* 5.5 and 8.6 Å, respectively, which offers tremendous possibilities for encapsulation of Keggin-type POM (diameters of *ca.* 13-14 Å).[26] Herein, a typical Keggin-type POM, $H_3PMo_{12}O_{40}$ has been adopted for direct encapsulated in the cavities of MIL-100(Fe) (denoted as HPMo@MIL-100(Fe)) *via* a simple one-pot hydrothermal method. Moreover, the as-obtained HPMo@MIL-100(Fe) nanocomposites exhibit much higher photocatalytic performance than those of original-MIL-100(Fe) or $H_3PMo_{12}O_{40}$ in two different processes, photocatalytic selective oxidation of alcohols and reduction of aqueous Cr(VI) under visible light irradiation (λ ≥ 420 nm). The origin accounting for the improved photoactivities and the underlying reaction mechanisms have been studied in terms of a series of characterization and trapping experiments. Moreover, the possible photocatalytic reactions mechanisms have also been investigated in detail.

2. Experimental

2.1. Reagents and chemicals

All reagents were analytical grade and used without further purification. phosphomolybdic acid ($H_3PMo_{12}O_{40}$), silver nitrate ($AgNO_3$), methanol, tert-butyl alcohol (TBA), potassium dichromate ($K_2Cr_2O_7$), and ethanol were purchased from Sinopharm Chemical Reagent Co., Ltd. (Shanghai, China). Iron (III) chloride hexahydrate ($FeCl_3•6H_2O$) was supplied by Aladdin Reagent Co., Ltd. (Shanghai, China). Trimethyl 1,3,5-benzenetricarboxylate was supplied by J&K Scientific Co., Ltd. (Beijing, China). Benzotrifluoride (BTF) (>99%) and benzyl alcohol (>99%) (BA) were supplied by Alfa Aesar China Co., Ltd. (Tianjin, China).

2.2. Synthesis of MIL-100(Fe)

MIL-100(Fe) was synthesized according to Canioni et al..[16] Briefly, $FeCl_3•6H_2O$ (0.378 g) and trimethyl 1,3,5-benzenetricarboxylate (0.272 g) were well mixed with 10 mL of deionized water in a Teflon liner. After stirred at 500 rpm for 30 min, the Teflon liner was sealed in a stainless steel autoclave and maintained at 130 °C for 72 h. After the heat treatment, the autoclave was allowed to cool naturally to room temperature, and the suspension was centrifuged at 4000 rpm for 5 min using a high speed centrifuge (TDL-5-A, Shanghai Anting Scientific Instrument Factory, China). A treatment in hot ethanol (60 °C) for 3 h was applied to decrease the amount of residual H_3BTC. Then, the obtained orange powder was centrifuged at 4000 rpm for 5 min and dried under vacuum at 100 °C for 12 h.

2.3. Fabrication of HPMo@MIL-100(Fe)

A certain amount of $H_3PMo_{12}O_{40}$ was first added into the mixture of MOF precursors. Then the rest of the procedure of resulting suspension was the same as that of MIL-100(Fe). In the reaction process, $H_3PMo_{12}O_{40}$ was encapsulated in the cavities of MIL-100(Fe). As-obtained samples were denoted as 2.5%HPMo@MIL-100(Fe), 5%HPMo@MIL-100(Fe), 10%HPMo@MIL-100(Fe), 20%HPMo@MIL-100(Fe), 30%HPMo@MIL-100(Fe) and 40%HPMo@MIL-100(Fe).

2.4. Characterizations

XRD patterns were carried on a Bruker D8 Advance X-ray diffrractometer operated at 40 kV and 40 mA with Ni-filtered Cu Ka irradiation (λ = 0.15406 nm). The data were recorded in the 2θ range of 3-50°. Thermo gravimetric analysis was carried out with a NETZSCH STA 449F3 unit at a heating rate of 5 °C/min under a nitrogen atmosphere. FT-infrared (FT-IR) spectra were carried out on a Nicolet 670 Fourier transform infrared spectrometer. Transmission electron microscopy (TEM) and high-resolution transmission electron microscopy (HRTEM) images were obtained using a JEOL model JEM 2010 EX instrument at an accelerating voltage of 200 kV. The elemental mapping over the desired region of the photocatalysts was detected by an energy-dispersive X-ray spectrometer (EDS) attached to the TEM. UV-vis diffuse reflectance spectra (UV-vis DRS) were obtained by a UV-vis spectrophotometer (Varian Cary 500). The Brunauer-Emmett-Teller (BET) surface area was measured with an ASAP2020M apparatus (Micromeritics Instrument Corp., USA). Before the test, the samples were degassed in vacuum at 120 °C for 6 hours. The nitrogen adsorption and desorption isotherms were measured at 77K. X-ray photoelectron spectroscopy (XPS) measurement was performed on a Thermo Scientific ESCA Lab 250 spectrometer which consists of a monochromatic Al Kα as the X-ray source, a hemispherical analyzer, and sample stage with multiaxial adjustability to obtain the surface composition of the sample. All of the binding energies were calibrated by the C 1s peak at 284.6 eV. The photoluminescence (PL) spectrum for samples were conducted on an Edinburgh

FL/FS900 spectrophotometer. The concentration of Fe(III) and Mo(VI) in the supernate was detected by the Ultima2 ICP optical emission spectrometer. The Mott-Schottky analysis and the electrochemical impedance spectroscopy (EIS) were performed at a Zahner electrochemical workstation. The photocurrent measurements were conducted on a Precision PARC workstation.

2.5. Evaluation of photocatalytic activity

The photocatalytic selective oxidation of various alcohols was performed as follows. A mixture of alcohol (0.1 mmol) and 20 mg of catalyst was dissolved in the solvent benzotrifluoride (BTF) (1.5 mL), which was saturated with pure molecular oxygen. The choice of the solvent BTF is because of its inertness to oxidation and high solubility for molecular oxygen. The above mixture was transferred to a 10 mL Pyrex glass bottle filled with molecular oxygen at a pressure of 0.1 MPa and stirred to make the catalyst blend evenly in the solution. For photocatalytic reaction under visible light irradiation, the reactor was irradiated by a 300 W Xe arc lamp (PLS-SXE 300, Beijing Perfectlight) with a UV-CUT filter to cut off light of wavelength < 420 nm. After the reaction, the mixture was centrifuged at 4000 rpm for 5 min to remove the catalyst particles completely. The remaining solution was analyzed with an Agilent Gas Chromatograph (GC-6820). Active species trapping experiments using different radical scavengers (methanol as scavenger for photogenerated holes,[18] $AgNO_3$ as scavenger for electrons[27,28] and tert-butyl alcohol (TBA) as scavenger for hydroxyl radical species[29]) were performed similar to the photocatalytic oxidation of benzyl alcohol except that the radical scavengers (0.1 mmol) were added to the reaction system. Conversion of alcohol and yield of aldehyde, and selectivity for aldehyde were defined as follows:

Conversion (%) = $[(C_0 - C_{BA}) / C_0] \times 100$

Yield (%) = $C_{BAD} / C_0 \times 100$

Selectivity (%) = $[C_{BAD} / (C_0 - C_{BA})] \times 100$

Where C_0 is the initial concentration of benzyl alcohol and C_{BA} and C_{BAD} are the concentrations of benzyl alcohol and benzaldehyde, respectively, at a certain time after the photocatalytic reaction.

For the photocatalytic reduction of aqueous Cr(VI), an ozone-free 300 W Xe lamp (PLS–SXE 300, Trusttech Co. Ltd., Beijing) with 420 nm cut-off filter was used as the light source (420 nm ≤ λ≤ 760 nm). In the photocatalytic activity text, 40 mg of photocatalyst was suspended in 40 mL of 20 mg•L^{-1} Cr(VI) aqueous solution. The pH value of reaction solution (pH 4) was adjusted with 2 mol•L^{-1} H_2SO_4. After adding of 5 mg hole scavenger (ammonium oxalate), the suspension was stirred in the dark for 2 h to ensure the establishment of adsorption-desorption equilibrium. During illumination, 4 mL of suspension was taken from the reactor at a scheduled interval and centrifuged to separate the photocatalyst. The Cr(VI) content in the supernatant solution was determined colorimetrically at 540 nm using the diphenylcarbazide method (DPC) with a Cary 50 UV-vis spectrophotometer (Varian Co.).[30] Active species trapping experiments using $AgNO_3$ as scavenger for photogenerated electrons was carried out similar to the above photocatalytic reduction of Cr(VI), except that $AgNO_3$ was added to the reaction system.[27]

3. Results and discussion

3.1. Characterizations

The X-ray diffraction (XRD) patterns of the as-synthesized MIL-100(Fe) and HPMo@MIL-100(Fe) nanocomposites are shown in Fig. 1. It is obvious that the XRD pattern of the MIL-100(Fe) is in good agreement with the calculated one (see Fig. S1). For HPMo@MIL-100(Fe) nanocomposites, when increasing the dosage of $H_3PMo_{12}O_{40}$, the intensities of diffraction peak (range from 3° to 8°) reducing gradually, suggesting that the pores of MIL-100(Fe) might be occupied. The similar phenomenon is also observed in the previously reported.[16] Moreover, no diffraction peaks for the original-$H_3PMo_{12}O_{40}$ can be observed in the HPMo@MIL-100(Fe) nanocomposites. This is probably due to the following two reasons: (i) the size of $H_3PMo_{12}O_{40}$ clusters are relatively small (*ca.* 13-14 Å); (ii) the $H_3PMo_{12}O_{40}$ clusters have been encapsulated in the cavities of MIL-100(Fe). Notably, when the amount of $H_3PMo_{12}O_{40}$ is more than 30 wt%, the XRD pattern of the sample would keep unchanged. Thus, it can be inferred that the loading amount of $H_3PMo_{12}O_{40}$ reached to the maximum when 30 wt%

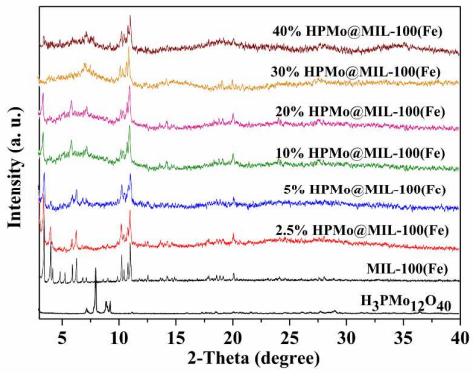

Fig. 1 XRD patterns of MIL-100(Fe) and HPMo@MIL-100(Fe) nanocomposites.

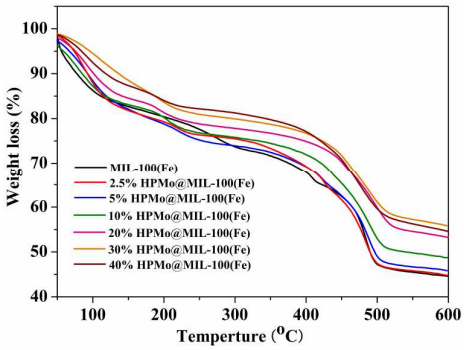

Fig. 2 TG curves of MIL-100(Fe) and HPMo@MIL-100(Fe) nanocomposites.

$H_3PMo_{12}O_{40}$ is used in the synthesis of the composite materials, which can be further evidenced by the thermogravimetric (TG) analysis. TG analyses of as-prepared samples are shown in Fig. 2. A first weight loss up to 100 °C corresponds to the departure of free water molecules, while water molecules in stronger interaction with the framework and/or POM moieties leave between 100 and 200 °C. As expected, at a temperature of 600 ºC, HPMo@MIL-100(Fe) exhibits a lower weight loss than that of MIL-100(Fe), indicating the successful encapsulation of $H_3PMo_{12}O_{40}$ in the MIL-100(Fe). Apparently, for 30%HPMo@MIL-100(Fe), about 55.7 wt% of the material remained, which is even higher than that of 30%HPMo@MIL-100(Fe) (54.9 wt%). Thus, we can envision that the maximal $H_3PMo_{12}O_{40}$ loading amount in HPMo@MIL-100(Fe) is 30%. Furthermore, inductively coupled plasma optical emission spectroscopy (ICP) measurements (see Table S1) of HPMo@MIL-100(Fe) exhibit a considerable loading capacity of $H_3PMo_{12}O_{40}$. It is worth noting that the experimental Mo/Fe ratio of 30%HPMo@MIL-100(Fe) is 0.4575, close to *ca.* 31.33 $H_3PMo_{12}O_{40}$ per unit cell (containing 816Fe). In addition, the BET surface area and pore structure of the prepared samples have been investigated (see Fig. S2 and Table 1). It can be seen that the BET surface area and pore volume decrease from 2006 to 302 m^2/g and from 0.9078 to 0.1601 cm^3/g for MIL-100(Fe) and 30%HPMo@MIL-100(Fe), respectively, in agreement with the presence of heavy phosphomolybdate moieties. Moreover, the results show that the BET surface area is 295 m^2/g of 40%HPMo@MIL-100(Fe), which is very similar to that of 30%HPMo@MIL-100(Fe).

Table 1 The BET surface area and pore volume of MIL-100(Fe) and HPMo@MIL-100(Fe) nanocomposites.

Sample	BET Surface Area (m^2/g)	Pore Volume (cm^3/g)
MIL-100(Fe)	2006	0.9078
2.5%HPMo@MIL-100(Fe)	1326	0.6901
5%HPMo@MIL-100(Fe)	1262	0.6701
10%HPMo@MIL-100(Fe)	957	0.4984
20%HPMo@MIL-100(Fe)	358	0.1803
30%HPMo@MIL-100(Fe)	302	0.1601
40%HPMo@MIL-100(Fe)	295	0.1595

Fig. 3 shows the Fourier transformed infrared spectroscopy (FTIR) spectra of $H_3PMo_{12}O_{40}$, MIL-100(Fe) and 30%HPMo@MIL-100(Fe). The vibrational bands of MIL-100(Fe) around 1456, 1376, 759, 711 cm^{-1}, and the peaks of the $H_3PMo_{12}O_{40}$ located at 1115, 1058, 960, 884, 819 cm^{-1} were all observed in the FTIR spectrum of the HPMo@MIL-100(Fe), which confirmed the presence of the MIL-100(Fe) and $H_3PMo_{12}O_{40}$ in the composite HPMo@MIL-100(Fe). Moreover, for HPMo@MIL-100(Fe), the ν_{as}(P-O_a) and ν_{as}(Mo-O_c) vibration bands (1058 and 819 cm^{-1}, respectively) are slightly shifted in comparison to free molybdophosphate (1061 and 790 cm^{-1}, respectively). This shift discloses the confinement effect of POM inside the porous solid.[31] The elemental composition and electronic structure of the MIL-100(Fe) and 30%HPMo@MIL-100(Fe) were investigated by X-ray photoelectron spectroscopy (XPS). The survey spectrum (see Fig. 4(a)) shows the existence of Fe, O, C, P and Mo in the HPMo@MIL-100(Fe). Regarding both two samples, the high-resolution XPS spectrum of the O 1s could be fitted by two peaks (532.2 and 531.2 eV) (see Fig. 4(b)), which are attributed to the oxygen components in the BTC linkers and the Fe-O bonds, respectively.[32,33] For HPMo@MIL-100(Fe), the binding energy located at 530.3 eV is assigned to the Mo-O bonds,[34] indicating that the $H_3PMo_{12}O_{40}$ molecules are successfully immobilized in the MIL-100(Fe). The doublet with binding energies of 232.2 (Mo $3d_{5/2}$) and 235.6 eV (Mo $3d_{3/2}$) in HPMo@MIL-100(Fe) further confirms the existence of $H_3PMo_{12}O_{40}$ (see Fig. 4(c)). Observation of the Fe 2p spectrum (see Fig. 4(d)), the binding energies of 712.1 and 726.0 eV are characteristic of Fe(III) in these two samples. The peak separation, namely, $\Delta = 2p_{1/2} - 2p_{3/2} = 14.1$ eV, which is very similar to those reported for α-Fe_2O_3.[35] The morphologies

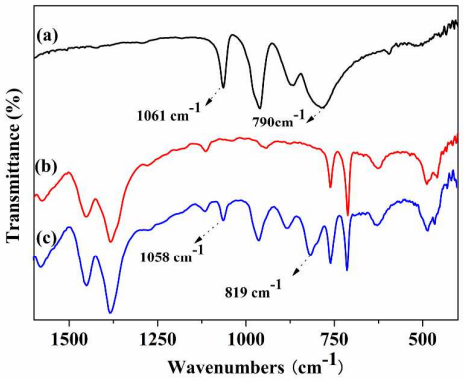

Fig. 3 IR spectra of (a) $H_3PMo_{12}O_{40}$, (b) MIL-100(Fe) and (c) 30%HPMo@MIL-100(Fe).

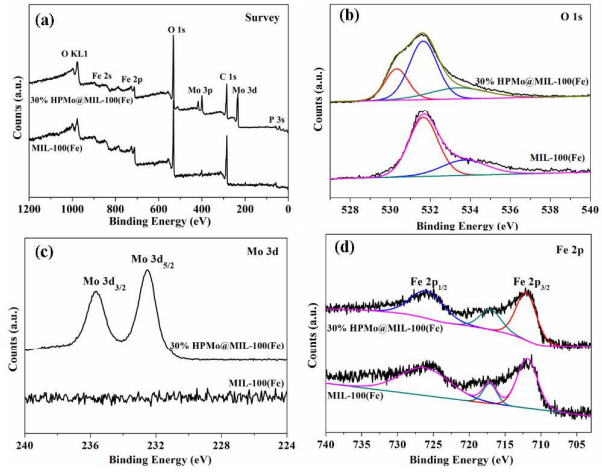

Fig. 4 XPS patterns of MIL-100(Fe) and 30%HPMo@MIL-100(Fe).

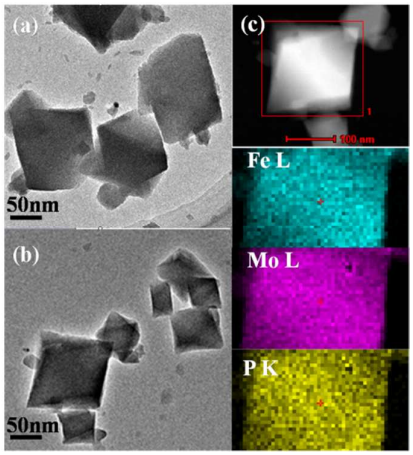

Fig. 5 TEM images of (a) MIL-100(Fe), (b) 30%HPMo@MIL-100(Fe) and (c) The mapping images of 30%HPMo@MIL-100(Fe).

of the samples have been determined by transmission electron microscopy (TEM). Fig. 5(a) and (b) shows typical TEM images of the sample MIL-100(Fe) and HPMo@MIL-100(Fe). It can be seen that the integrity of characteristic structure of MIL-100(Fe) is retained and not influenced by the encapsulation of $H_3PMo_{12}O_{40}$. Notably, no characteristic diffractions for $H_3PMo_{12}O_{40}$ clusters can beobserved in the HPMo@MIL-100(Fe) nanocomposite (see Fig. S3(a)), implying that the $H_3PMo_{12}O_{40}$ clusters have been encapsulated in HPMo@MIL-100(Fe). The EDS elemental mapping also confirms that Fe, P and Mo elements are uniformly distributed in the HPMo@MIL-100(Fe) (see Fig. 5(c) and Fig. S3(b)).

As the photoabsorption property plays a key role in determining the photocatalytic activity, the UV-vis diffuse reflectance spectra (DRS) of the samples have been measured. It can be observed from Fig. 6 that, with regard to all the samples, an intense UV absorption band appears at 320 nm is assigned to the ligand-to-metal charge transfer (LMCT), implying the bonding of carboxylate oxygen to metal ($^6A_{1g}$ => $^4A_{1g}$ + $^4Eg(G)$) in Fe(III).[36] Moreover, the absorption spectra of HPMo@MIL-100(Fe) nanocomposites exhibit the strong

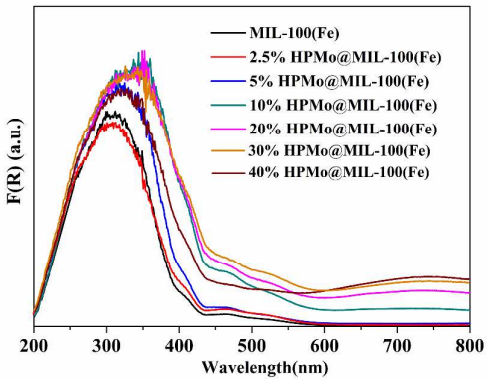

Fig. 6 UV-vis DRS spectra of MIL-100(Fe) and HPMo@MIL-100(Fe) nanocomposites.

absorption bands in the range of 400-500 nm, which can be attributed to absorption induced by LMCT of O(II) → Mo(VI), suggesting the presence of $H_3PMo_{12}O_{40}$.[37] Furthermore, a qualitative red shift to higher wavelength is observed in the absorption edge of all HPMo@MIL-100(Fe) nanocomposites, which might be attributed to the electronic interactions between $H_3PMo_{12}O_{40}$ and MIL-100(Fe). Obviously, the HPMo@MIL-100(Fe) nanocomposites possess much better visible light absorption intensity than MIL-100(Fe). Thus, we can envision that the introduction of $H_3PMo_{12}O_{40}$ may lead to the enhancement of the MOFs' photocatalytic activity for a target reaction.

3.2. Photocatalytic properties

Photocatalytic selective oxidation of alcohols. To investigate the visible light photoactivities of HPMo@MIL-100(Fe) nanocomposites, the selective oxidation of benzyl alcohol using molecular oxygen as an oxidant has been carried out because the transformation of alcohols to aldehydes remains an important task in many important industrial and fine chemicals production processes.[38,39] Control experiments have been first carried out to demonstrate the photocatalytic nature of the reactions. As shown in Fig. 7(a), control experiments in the absence of catalyst or light lead to no conversion of substrate alcohols, which ensures that the reaction is driven by a photocatalytic process. Besides, a control experiment in the N_2-saturated atmosphere shows that almost no benzyl alcohol has been transferred, indicating that oxygen is the primary oxidant for the photocatalytic oxidation

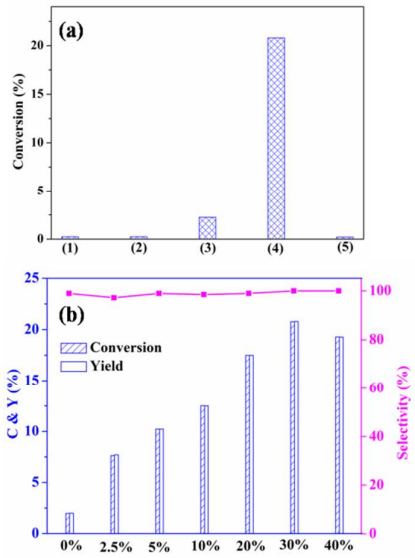

Fig. 7 (a) Control experiments for the transformation of benzyl alcohol (0.1 mmol in 1.5 mL BTF) under different conditions; the reaction time is 4 h. Entry 1: 30%HPMo@MIL-100(Fe) + O_2, in the dark; 2: no catalyst, visible light; 3: 30%HPMo@MIL-100(Fe) + N_2, visible light; 4: 30%HPMo@MIL-100(Fe) + O_2, visible light; 5: 30%HPMo@MIL-100(Fe) under 80 °C, in the dark, (b) Visible light photocatalytic selective oxidation of benzyl alcohol over the HPMo@MIL-100(Fe) nanocomposites prepared with different $H_3PMo_{12}O_{40}$ loading amount.

system. To exclude the heating effect, the experiment has been also carried out at 80°C in the darkness, yielding negligible amounts of aldehyde products, which confirms the oxidation of benzylic alcohols is not a thermal catalytic reaction. Moreover, it is also crucial to control the content of $H_3PMo_{12}O_{40}$ to achieve an optimal synergy interaction between $H_3PMo_{12}O_{40}$ and MIL-100(Fe) for selective oxidation of alcohols. Taking a view of the overall activities from Fig. 7(b), it can be found that the conversion to values (*ca.* 21.0%) in all the samples, and notably, the selectivity to benzaldehyde is nearly 100%. It is reasonable because $H_3PMo_{12}O_{40}$ is the major catalyst during this reaction, and the porous MIL-100(Fe) mainly acting as the support for $H_3PMo_{12}O_{40}$ (only 2.1% aldehydes conversion). The bulk-$H_3PMo_{12}O_{40}$ disperses unevenly in BTF, resulting in low conversion of alcohols. However, for HPMo@MIL-100(Fe), the $H_3PMo_{12}O_{40}$ clusters within MIL-100(Fe) can behave as quantum dots. These $H_3PMo_{12}O_{40}$ quantum dots might exhibited higher photoactivity than that of bulk-$H_3PMo_{12}O_{40}$.[40] As a result, the benzaldehyde conversion will increase rapidly by the increasing $H_3PMo_{12}O_{40}$ loading amount. Furthermore, the photoactivity of 30%HPMo@MIL-100(Fe) nanocomposite is higher than that of MIL-100(Fe), $H_3PMo_{12}O_{40}$ and HPMo-MIL-100(Fe) which is prepared by simply mixing $H_3PMo_{12}O_{40}$ and MIL-100(Fe) in proper proportions under identical conditions (see Fig. 8). In addition, 30%HPMo@MIL-100(Fe) exhibits high photocatalytic activity for selective oxidation of a range of benzylic alcohols with various substituent groups to their corresponding aldehydes under the irradiation of visible light (λ ≥ 420 nm). As summarized in Table 2, it is clear to see that these alcohols can be transformed to aldehydes with high selectivity (90~100%). The difference in the photoactivity toward selective transformation of alcohols can be attributed to the following two reasons: (i) benzylic alcohols with various substituents (electron donating/accepting group) could affect the conversion; (ii) the different adsorption capacity of benzylic alcohols with various substituents on the surface of the photocatalyst.

Since the nanocomposites of 30%HPMo@MIL-100(Fe) show the best photocatalytic performance in the selective oxidation of benzyl alcohol to benzaldehyde under the visible light irradiation. Thus we chose this material to evaluate the

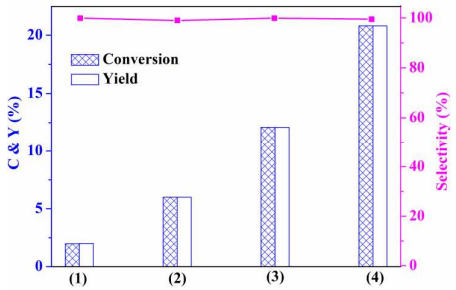

Fig. 8 Photocatalytic selective oxidation of benzyl alcohol over (1) MIL-100(Fe), (2) $H_3PMo_{12}O_{40}$, (3) 30%HPMo-MIL-100(Fe), (4) 30%HPMo@MIL-100(Fe) under the irradiation of visible light for 4 hours (λ ≥ 420 nm).

Table 2 Photocatalytic aerobic oxidation of various alcohols on 30%HPMo@MIL-100(Fe) under the irradiation of visible light (λ ≥ 420 nm)[a].

Entry	Substrate	Product	Conv. [%]	Sel. [%]
1	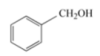		21.0	>99
2	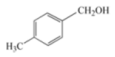	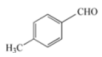	13.3	97
3	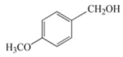	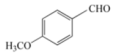	8.0	>99
4	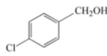	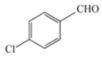	18.0	>99
5	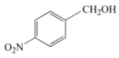	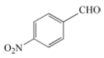	20.4	>99
6	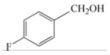		29.1	93

[a] Reaction conditions: alcohol (0.1 mmol) and 20 mg 30%HPMo@MIL-100(Fe) were stirred in 1.5 mL of BTF under 0.1 MPa O_2 under visible light irradiation (λ ≥ 420 nm) for 4 h.

stability and reusability of the HPMo@MIL-100(Fe) photocatalysts. After each cycling experiment, the photocatalyst was separated from the aqueous suspension by filtration, washed with ethanol and deionized water several times to completely remove the absorbed benzyl alcohol on the surface of sample. And then, the photocatalyst was centrifuged and dried under vacuum at 100 °C for 5 h. As shown in Fig. S4(a), no noticeable activity change is observed during four successive recycles, suggesting that the HPMo@MIL-100(Fe) possesses high stability and reusability during the photocatalytic selective oxidation reaction. Moreover, XRD patterns (see Fig. S4(b)) of the fresh and used samples reveal an intact crystalline structure of the 30%HPMo@MIL-100(Fe) after cycling experiments. Additionally, the amount of Fe and Mo ions leaching during the reaction has been quantified by ICP optical emission spectrometer. Apparently, there is almost no Fe and Mo ions leaching from the HPMo@MIL-100(Fe) during the reaction (see Table S2).

To gain more insight into the reaction, active species trapping experiments have been taken to explore the photoactive species during selective oxidation of benzylic alcohols over HPMo@MIL-100(Fe). As shown in Fig. 9, the addition of $AgNO_3$ (an electron scavenger) could induce the depression effect on the photocatalytic selective oxidation of alcohols. About 7.9% inhibition is observed when $AgNO_3$ is added to photocatalytic reaction systems (see entry 2). It can be speculated that the photogenerated electrons over HPMo@MIL-100(Fe) are involved in the formation of photocatalytic active species, that is, superoxide radical species ($\bullet O_2^-$). A similar and obvious inhibition phenomenon for photocatalytic reaction is also observed when methanol (a scavenger of photogenerated holes) is added into the reaction

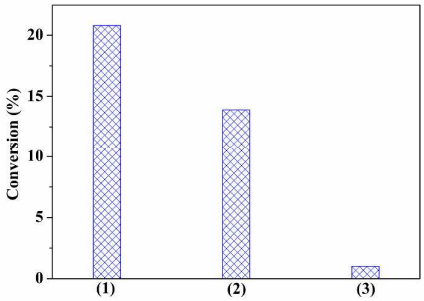

Fig. 9 The photocatalytic selective oxidation of benzyl alcohol over the 30%HPMo@MIL-100(Fe) under visible light irradiation in the presence of radical scavengers (1: no additives, 2: $AgNO_3$, 3: methanol).

system (see entry 3). This obvious inhibitory effect of methanol means that photogenerated holes are the main contributors to the photocatalytic process.

In order to understand the causes for enhancing the photocatalytic performance of the 30%HPMo@MIL-100(Fe), we have performed the photoelectrochemical experiments. Fig. 10(a) displays the photocurrent transient response of MIL-100(Fe) and 30%HPMo@MIL-100(Fe) under intermittent visible light illumination (λ ≥ 420 nm). It is clear to see that the 30%HPMo@MIL-100(Fe) shows a strong photocurrent response and the photocurrent rapidly decreases to zero as long as the light is switched off. This indicates a more efficient separation of the photoexcited electron-hole pairs and longer lifetime of the photogenerated charge carriers, which can be further proved by the photoluminescence (PL) results. Under 250 nm laser irradiation at room temperature, MIL-100(Fe) shows a broad PL peak centered at 375 nm (Fig. 10(b)), which is attributed to the benzene-1,3,5-tricarboxylic acid linkers in MIL-100(Fe) structure.[41] Moreover, the PL intensity obtained over 30%HPMo@MIL-100(Fe) is much weaker than that of MIL-100(Fe), suggesting the longer lifetime of photogenerated charge carriers in 30%HPMo@MIL-100(Fe). To further determine the advantage of 30%HPMo@MIL-100(Fe) over MIL-100(Fe) in improving the charge-carriers transfer, electrochemical impedance spectra (EIS) Nyquist plot, a very useful tool to characterize the charge-carriers migration, has also been performed (see Fig. 10(c)).[42,43] Obviously, the 30%HPMo@MIL-100(Fe) exhibits depressed impedance arc radius compared with original-MIL-100(Fe), suggesting that $H_3PMo_{12}O_{40}$ can benefit to promote the interfacial charge transfer, which is in line with its higher photocurrent transient response under visible light irradiation.

Electrochemical analysis of the MIL-100(Fe) has been carried out in our previous work (see Fig. S5). It can be obtained that the flat-band potential of the MIL-100(Fe) is around -0.60 V *vs.* Ag/AgCl at pH 6.8, corresponding to a potential of -0.40 V *vs.* NHE at pH 6.8, which is more negative than the standard reduction potential of oxygen (-0.15 V *vs* NHE).[44] Therefore, it is thermodynamically permissible for the transformation of photogenerated electrons to the absorbed O_2 to produce the $\bullet O_2^-$. Moreover, the flat-band potential of

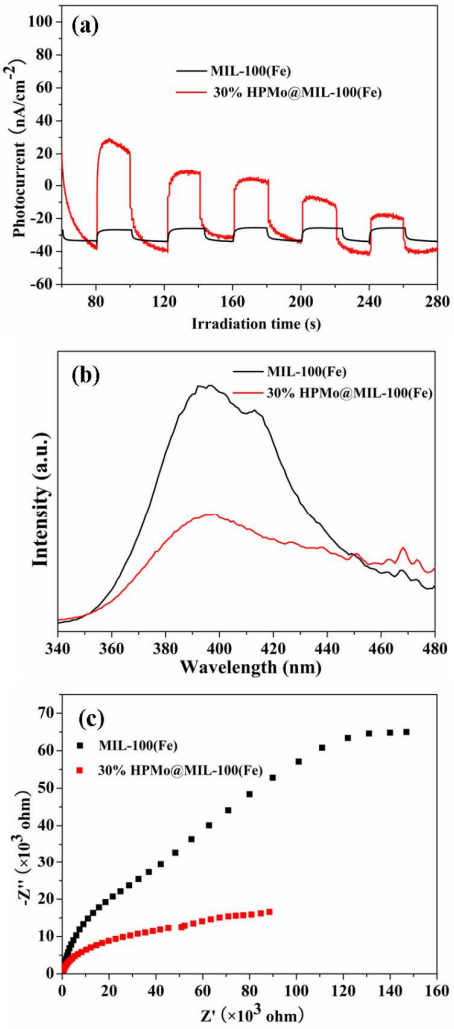

Fig. 10. (a) Transient photocurrent response of MIL-100(Fe) and 30%HPMo@MIL-100(Fe) in 0.2 M Na_2SO_4 aqueous solution (pH 6.8) versus Ag/AgCl under visible light irradiation (λ ≥ 420 nm), (b) Photoluminescence (PL) spectra of MIL-100(Fe) and 30%HPMo@MIL-100(Fe) (c) Nyquist impedance plots of MIL-100(Fe) and 30%HPMo@MIL-100(Fe).

$H_3PMo_{12}O_{40}$ is around -0.28 V *vs*. NHE.[45] Combining with the band gap energy estimated from UV-vis DRS spectra (see Fig.S6), the calculated conduction band potential (V_{CB}) is equal to 2.09 V *vs.* NHE. The matched band potentials between HPMo@MIL-100(Fe) and $H_3PMo_{12}O_{40}$ make it theoretically feasible for MIL-100(Fe) to transfer the photogenerated electrons from its CB to $H_3PMo_{12}O_{40}$ under visible light irradiation, thus, effective transportation of the photogenerated electrons and holes could be achieved. Accordingly, a possible mechanism for photocatalytic selective oxidation of benzylic alcohols over the HPMo@MIL-100(Fe) nanocomposites can be proposed in Fig. 11. That is, under the visible light irradiation, the adsorbed benzyl alcohol in solution interacts with holes to form the corresponding radical cations, which further reacts with dioxygen or superoxide radicals, leading to the formation of corresponding aldehydes.

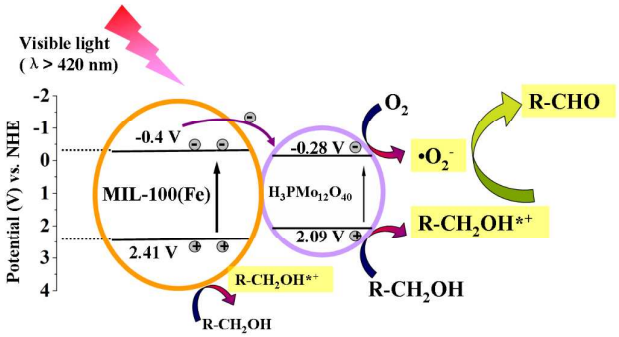

Fig. 11 Proposed mechanism for the photocatalytic selective oxidation of benzyl alcohol over HPMo@MIL-100(Fe) under visible light irradiation (λ ≥ 420 nm).

Photocatalytic reduction of Cr(VI). The photocatalytic performance of HPMo@MIL-100(Fe) can be further evidenced by the photocatalytic reduction of hexavalent chromium (Cr(VI)) to Cr(III) in aqueous solution. Cr(VI) is a frequent contaminant in wastewater arising from industrial processes such as leather tanning, paint making, and so on. Its removal from wastewater is of crucial importance because it is harmful to biological systems and can easily get into the food chains.[46,47] Control experiments (without photocatalyst or visible light) reveal negligible photocatalytic activities, verifying that the photocatalytic reduction reaction is truly driven by a photocatalytic process (see Fig. 12(a)). Moreover, it can be found that the reduction of Cr(VI) hardly occurs in the presence of $H_3PMo_{12}O_{40}$. As mention above, the CB of $H_3PMo_{12}O_{40}$ is -0.28 V *vs.* NHE, which is more negative than the Cr(VI)/Cr(III) potential (+0.51 V *vs.* NHE).[14] It is thermodynamically permissible for the reduction of Cr(VI) over $H_3PMo_{12}O_{40}$. However, it should be noted that $H_3PMo_{12}O_{40}$ molecules are with negative charge in aqueous solution due to the dissolved H^+. On other hand, at pH 2-7, the predominating species of chromium is $Cr_2O_7^{2-}$. Therefore, the negative charge on $H_3PMo_{12}O_{40}$ would electrostatically repel the $Cr_2O_7^{2-}$ anions. As a result, photogenerated electrons cannot transfer to $Cr_2O_7^{2-}$ effectively, and the photocatalytic activity decreases. Taking a view of the overall activities from Fig. 12(b), it can be found that different from the case of photocatalytic selective oxidation of alcohols discussed above, the optimal $H_3PMo_{12}O_{40}$ content is found to be 5 wt%. After 8 min of visible light illumination, almost 100% Cr(VI) can be reduced. The major reason for the different optimal content of $H_3PMo_{12}O_{40}$ is due to the active components difference. That is, in this system, MIL-100(Fe) plays a major role for the reduction of Cr(VI). Because the positively charge surface of MIL-100(Fe) will be more beneficial to adsorb $Cr_2O_7^{2-}$ anionic, and then enhances the reaction rate (see Fig. S7). Thus, the excessive encapsulation of cocatalyst $H_3PMo_{12}O_{40}$ in the nanocomposites would decrease the amount of reaction centers and lower catalytic sites, resulting in lower reaction rate. Moreover, we have also tested the photoactivity of MIL-100(Fe), commercial $H_3PMo_{12}O_{40}$ and HPMo-MIL-100(Fe) under identical experimental conditions, respectively (see Fig. S8). As expected, HPMo@MIL-100(Fe) exhibits the highest photoactivity. In addition, the stability of HPMo@MIL-100(Fe) for the photocatalytic reduction of Cr(VI) has also been studied. As reflected by the recycled testing results in Fig. 13, HPMo@MIL-100(Fe) exhibit satisfying stability, which can be further evidenced by the ICP analysis (see Table S3).

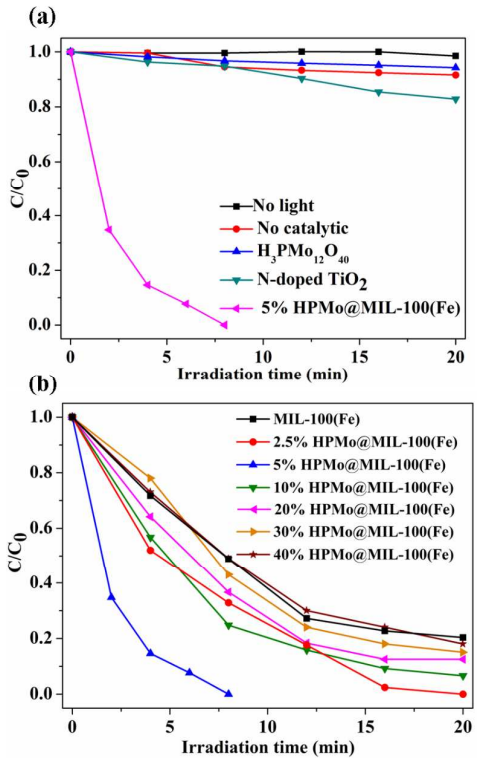

Fig. 12 (a) Control experiments of photocatalytic reduction of Cr(VI) under different conditions, (b) Photocatalytic reduction of aqueous Cr(VI) over HPMo@MIL-100(Fe). Reaction conditions: 40 mg of photocatalyst, 40 mL of 20 mg·L^{-1} Cr(VI), 5 mg of ammonium oxalate, pH 4.

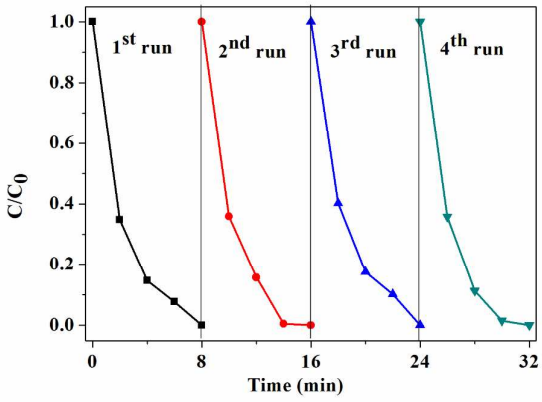

Fig. 13 Reusability of HPMo@MIL-100(Fe) for the photocatalytic reduction of Cr(VI).

To ensure the decisive role of photogenerated electrons during reduction of Cr(VI), we have performed the controlled experiments, using $AgNO_3$ as scavenger for photogenerated electrons, for reduction of Cr(VI) over HPMo@MIL-100(Fe) under visible light irradiation. The results are displayed in Fig.

S9, it is clear to see that almost no Cr(VI) can be restored, which clearly indicates that the photoreduction of Cr(VI) is driven by photogenerated electrons. Combining with photoelectrochemical analyses (see Fig. S10), it could be revealed that the encapsulation of $H_3PMo_{12}O_{40}$ in the pores of MIL-100(Fe) can effectively improve charge-separation efficiency of MIL-100(Fe) under visible-light irradiation (λ ≥ 420 nm). This in turn leads to the enhancement of visible-light-driven photoactivity of 5%HPMo@MIL-100(Fe) toward photocatalytic reduction of Cr(VI). Accordingly, a probable mechanism for the reduction of Cr(VI) over HPMo@MIL-100(Fe) has been proposed. Under visible light irradiation (λ ≥ 420 nm), the photogenerated charge carriers migrate to the surface of the MIL-100(Fe) and participate in the redox reaction. Due to the presence of $H_3PMo_{12}O_{40}$, the photogenerated charge-carrier can be separated more efficiently. The photogenerated electrons can reduce Cr(VI) to Cr(III). The photogenerated positive holes are scavenged by the quenching agent of ammonium oxalate, thus offering an adequate opportunity of spatial contact between photogenerated electrons and Cr(VI).

4. Conclusions

In summary, a series of HPMo@MIL-100(Fe) nanocomposites have been fabricated *via* a facile hydrothermal approach by simply one-pot encapsulation of $H_3PMo_{12}O_{40}$ in the pores of MIL-100(Fe). Results demonstrate that the as-prepared HPMo@MIL-100(Fe) nanocomposites are stable and able to serve as a promising photocatalyst for the selective oxidation of alcohols and reduction of heavy metal ions Cr(VI) under visible light irradiation (λ ≥ 420 nm). In contrast to MIL-100(Fe), HPMo@MIL-100(Fe) nanocomposites exhibit enhanced photocatalytic performance for both of the oxidation and reduction processes. The higher photoactivity of HPMo@MIL-100(Fe) nanocomposites can be ascribed to the synergistic effect of the enhanced light absorption intensity and more efficient separation of the charge-carrier. The optimal $H_3PMo_{12}O_{40}$ contents are found to be 30 wt% and 5 wt% for the selective oxidation and reduction processes, respectively, giving a 21.0% aldehydes conversion and 100% Cr(VI) reduction ratio under visible light irradiation. The major reason for the difference of optimal $H_3PMo_{12}O_{40}$ content is due to the active components difference. That is, in selective oxidation system, $H_3PMo_{12}O_{40}$ serves as the major photocatalyst. In Cr(VI) reduction process, the photoactive MIL-100(Fe) plays the key role. This is the first report on the systematic study of photocatalytic performance of POM@MOFs nanocomposites. It is hoped that our current work could widen the application range of the MOFs as well as offer new inroads into exploration and utilization of MOF-based nanocomposites as visible light photocatalysts for solar energy conversion.

Acknowledgements

This work was supported by the National Natural Science Foundation of China (21273036 and 21177024) and Science & Technology Plan Project of Fujian Province (2014Y2003).

Notes and references

1 D. Sattari and C. L. Hill, *J. Am. Chem. Soc.*, 1993, **115**, 4649-4657.
2 A. Hiskia, A. Mylonas and E. Papaconstantinou, *Chem. Soc. Rev.*, 2001, **30**, 62-69.
3 W. Alharbi, E. Brown, E. F. Kozhevnikova and I. V. Kozhevnikov, *J. Catal.*, 2014, **319**, 174-181.
4 S. Herrmann, C. Ritchie and C. Streb, *Dalton Trans.*, 2015, **44**, 7092-7104.
5 Y. Guo, Y. Wang, C. Hu, Y. Wang, E. Wang, Y. Zhou and S. Feng, *Chem. Mater.*, 2000, **12**, 3501-3508.
6 C. Chen, P. Lei, H. Ji, W. Ma, J. Zhao, H. Hidaka and N. Serpone, *Environ. Sci. Technol.*, 2004, **38**, 329-337.
7 S. Zhao, Y. Jia and Y.-F. Song, *Catal. Sci. Tech.*, 2014, **4**, 2618-2625.
8 T. Baba and Y. Ono, *Appl. Catal.*, 1986, **22**, 321-324.
9 S. Lim, Y. Kim, G. Park, W. Lee, I. Song and H. Youn, *Catal. Lett.*, 1999, **60**, 199-204.
10 I. V. Kozhevnikov, K. R. Kloetstra, A. Sinnema, H. W. Zandbergen and H. van Bekkum, *J. Mol. Catal. A: Chem.*, 1996, **114**, 287-298.
11 Y. Shiraishi, T. Naito and T. Hirai, *Ind. Eng. Chem. Res.*, 2003, **42**, 6034-6039.
12 G. Ferey, *Chem. Soc. Rev.*, 2008, **37**, 191-214.
13 X. Si, J. Zhang, F. Li, C. Jiao, S. Wang, S. Liu, Z. Li, H. Zhou, L. Sun and F. Xu, *Dalton Trans.*, 2012, **41**, 3119-3122.
14 R. Liang, L. Shen, F. Jing, W. Wu, N. Qin, R. Lin and L. Wu, *Appl. Catal. B: Environ.*, 2015, **162**, 245-251.
15 C.-Y. Sun, S.-X. Liu, D.-D. Liang, K.-Z. Shao, Y.-H. Ren and Z.-M. Su, *J. Am. Chem. Soc.*, 2009, **131**, 1883-1888.
16 R. Canioni, C. Roch-Marchal, F. Secheresse, P. Horcajada, C. Serre, M. Hardi-Dan, G. Ferey, J.-M. Greneche, F. Lefebvre, J.-S. Chang, Y.-K. Hwang, O. Lebedev, S. Turner and G. Van Tendeloo, *J. Mater. Chem.*, 2011, **21**, 1226-1233.
17 E. V. Ramos-Fernandez, C. Pieters, B. van der Linden, J. Juan-Alcañiz, P. Serra-Crespo, M. W. G. M. Verhoeven, H. Niemantsverdriet, J. Gascon and F. Kapteijn, *J. Catal.*, 2012, **289**, 42-52.
18 M. Alvaro, E. Carbonell, B. Ferrer, F. X. Llabres i Xamena and H. Garcia, *Chemistry*, 2007, **13**, 5106-5112.
19 L. Shen, S. Liang, W. Wu, R. Liang and L. Wu, *Dalton Trans.*, 2013, **42**, 13649-13657.
20 R. Liang, F. Jing, L. Shen, N. Qin and L. Wu, *J. Hazard. Mater.*, 2015, **287**, 364-372.
21 F. Zhang, Y. Jin, J. Shi, Y. Zhong, W. Zhu and M. S. El-Shall, *Chem. Eng. J.*, 2015, **269**, 236-244.
22 L. E. Lange and S. K. Obendorf, *ACS Appl. Mater. Interfaces*, 2015, **7**, 3974-3980.
23 A.-X. Yan, S. Yao, Y.-G. Li, Z.-M. Zhang, Y. Lu, W.-L. Chen and E.-B. Wang, *Chem. Eur. J.* 2014, **20**, 6927-6933.
24 P. Horcajada, S. Surble, C. Serre, D.-Y. Hong, Y.-K. Seo, J.-S. Chang, J.-M. Greneche, I. Margiolaki and G. Ferey, *Chem. Commun.*, 2007, 2820-2822.
25 C.-F. Zhang, L.-G. Qiu, F. Ke, Y.-J. Zhu, Y.-P. Yuan, G.-S. Xu and X. Jiang, *J. Mater. Chem. A*, 2013, **1**, 14329-14334.
26 L. H. Wee, S. R. Bajpe, N. Janssens, I. Hermans, K. Houthoofd, C. E. Kirschhock and J. A. Martens, *Chem. Commun. (Camb.)*, 2010, **46**, 8186-8188.
27 C. Xing, Y. Zhang, Z. Wu, D. Jiang and M. Chen, *Dalton Trans.*, 2014, **43**, 2772-2780.
28 A. Kudo, K. Ueda, H. Kato and I. Mikami, *Catal. Lett.*, 1998, **53**, 229-230.

29 P. Wang, B. Huang, Y. Dai and M.-H. Whangbo, *Phys. Chem. Chem. Phys.*, 2012, **14**, 9813-9825.
30 A. Idris, N. Hassan, R. Rashid and A.-F. Ngomsik, *J. Hazard. Mater.*, 2011, **186**, 629-635.
31 Y. Guo, D. Li, C. Hu, E. Wang, Y. Zou, H. Ding and S. Feng, *Microporous Mesoporous Mater.*, 2002, **56**, 153-162.
32 S. K. Das, M. K. Bhunia, M. Motin Seikh, S. Dutta and A. Bhaumik, *Dalton Trans.*, 2011, **40**, 2932-2939.
33 S. K. Tam, J. Dusseault, S. Polizu, M. Ménard, J.-P. Hallé and L. H. Yahia, *Biomaterials*, 2005, **26**, 6950-6961.
34 A. K. Poswal, D. Bhattacharyya, S. N. Jha, Sangeeta and S. C. Sabharwal, *Bull. Mater. Sci.*, 2012, **35**, 103-106.
35 C. Yu, L. Gou, X. Zhou, N. Bao and H. Gu, *Electrochim. Acta*, 2011, **56**, 9056-9063.
36 S. Bordiga, C. Lamberti, G. Ricchiardi, L. Regli, F. Bonino, A. Damin, K. P. Lillerud, M. Bjorgen and A. Zecchina, *Chem. Commun.*, 2004, 2300-2301.
37 N. Dubey, S. S. Rayalu, N. K. Labhsetwar, R. R. Naidu, R. V. Chatti and S. Devotta, *Appl. Catal. A: Gen.*, 2006, **303**, 152-157.
38 M. Zhang, Q. Wang, C. Chen, L. Zang, W. Ma and J. Zhao, *Angew. Chem., Int. Ed.* , 2009, **48**, 6081-6084.
39 G. J. ten Brink, I. C. E. Arends and R. Sheldon, *Science*, 2000, **287** , 1636-1639.
40 X. Xing, R. Liu, X. Yu, G. Zhang, H. Cao, J. Yao, B. Ren, Z. Jiang and H. Zhao, *J. Mater. Chem. A*, 2013, **1**, 1488-1494.
41 M. D. Allendorf, C. A. Bauer, R. K. Bhakta and R. J. T. Houk, *Chem. Soc. Rev.*, 2009, **38**, 1330-1352.
42 D. Wang, D. Choi, J. Li, Z. Yang, Z. Nie, R. Kou, D. Hu, C. Wang, L. V. Saraf, J. Zhang, I. A. Aksay and J. Liu, *ACS Nano*, 2009, **3**, 907-914.
43 T. Lu, Y. Zhang, H. Li, L. Pan, Y. Li and Z. Sun, *Electrochim. Acta*, 2010, **55**, 4170-4173.
44 40.M. Zhang, C. Chen, W. Ma and J. Zhao, *Angew. Chem.*, 2008, **120**, 9876-9879.
45 N. Dubey, S. S. Rayalu, N. K. Labhsetwar and S. Devotta, *Int. J. Hydrogen Energy*, 2008, **33**, 5958-5966.
46 S. Zhang, M. Zeng, W. Xu, J. Li, J. Li, J. Xu and X. Wang, *Dalton Trans.*, 2013, **42**, 7854-7858.
47 Y. Ku and I.-L. Jung, *Water Res.*, 2001, **35**, 135-142.

Graphical Table of Contents

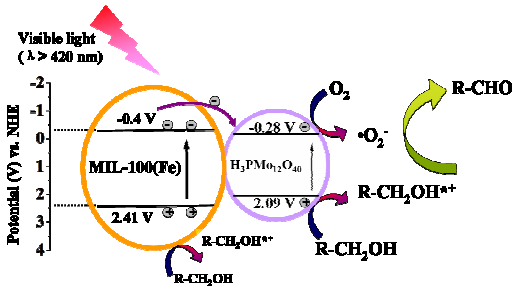

Multifunctional $H_3PMo_{12}O_{40}$ encapsulated in MIL-100(Fe) as dual functional visible-light-driven photocatalysts for selective transformation under visible light.